Physics Department, Trinity College, Dublin

Transfer Report

Student: Plamen Stamenov **Supervisor: Prof. J. M. D. Coey**

20/09/2004

Table of Contents

1 Abstract

Few subjects in science are more difficult to understand than magnetism.
***Encyclopedia Britanica*, Fifteenth Edition 1989.**

The development of the relatively new area of spin electronics depends upon the existence of materials and structures that may be used as effective spin-polarized current injectors, transmitters, manipulators and detectors. Potential high efficiency injectors include tunnel and Schottky barriers employing ferromagnetic and half-metals. As media with long carrier mean free path and spin-coherence length, an eventual transmitter, few possibilities are currently explored, including classical IV, III-V, II-VI semiconductors, and semimetals as bismuth and graphite. Various means are used to manipulate and detect spin-polarized currents – optical (magnetic circular dichroism and Kerr effect), electrostatic (FET with spin-orbit coupling) and galvanic (different types of Hall effect and magnetoresistance devices.

Hereafter, experiments devised to explore the first two bits in the above 'spin chain' will be described. Namely, the possibility to use Schottky barriers as efficient spin-injectors, including the more fundamental aspect of spin-polarisation measurement, and the fundamental properties of graphite (a good example of a semi-metal) and multi-walled carbon nanotubes, eventual nano-scale electronics building blocks.

In the first chapter a brief background on the subject will be provided. The standard results of the Schottky-Bethe theory of the metal-semiconductor junctions will be given, with extensions for spin-polarized metals. Graphite and its polymorphs will be described in terms of their physical properties.

The second chapter contains the main experimental results on the above two problems, with the conclusions drawn and a discussion of the possibilities for further investigations.

Following, list of the major experimental apparata constructed will be given with brief description, specifications and measurements capabilities.

2 Background on the Research Topics

2.1 Main results of the theory of Schottky Junctions

Spin electronics is a quickly growing field at the border between magnetism and semi-conductor physics, which is trying to exploit the spin-degree of freedom of the electron (or any other quasi-particle in the solid) to realize new devises with fundamentally new or enhanced properties. May be the first and the most common two terminal spin electronic device, the spin valve, consists of at least two ferromagnetic layers the magnetisation of which can be switched independently. The magnitude of the total current at a given bias is thus dependent on the mutual orientation of the magnetisations of the ferromagnetic layers, provided that the current flowing through the layers is at least partially spin-polarized. The actual static or current polarisation are given by:

$$\alpha_s = \frac{n_\uparrow - n_\downarrow}{n_\uparrow + n_\downarrow}$$

$$\alpha_c = \frac{n_\uparrow v_{F\uparrow} - n_\downarrow v_{F\downarrow}}{n_\uparrow v_{F\uparrow} + n_\downarrow v_{F\downarrow}},$$

the ratios being close to unity for the case of a half-metallic material.

Injection of spin-polarized currents into semi-conductors is problematic because of the conductivity mismatch or the vastly different Fermi surfaces. [2] There are several ways to avoid this problem, some of which are the injection of hot electrons through a tunnel barrier or Schottky barrier (metal-semiconductor contact at appropriate combination of the respective work functions).

In order to understand the potential of the Schottky junction as a spin-polarised current injector or a spin-filter one should analyse the main transport mechanisms visualized on Fig. 2-1.

[1] Where the different contributions are as follows:

a) Thermo-ionic emission of electrons from the semiconductor over the top of the barrier into the semiconductor;
b) Quantum-mechanical tunnelling through the barrier;
c) Recombination in the space-charge region;
d) Recombination in the neutral region.

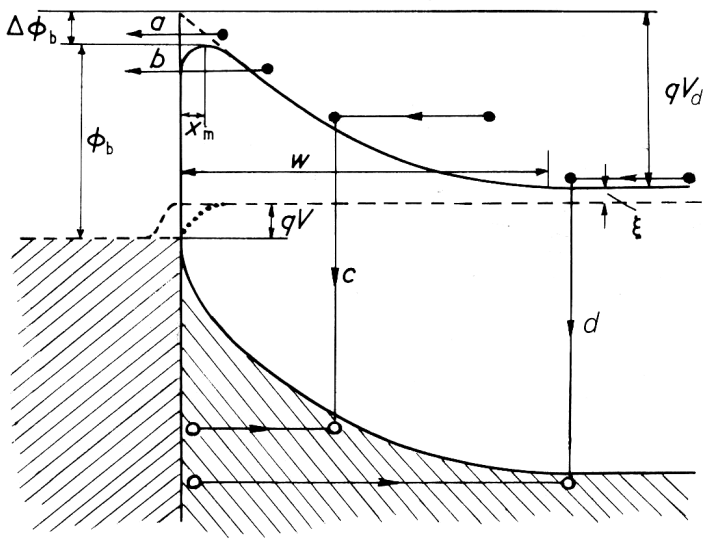

Figure 2-1 Various current contributions in a Schottky barrier

There are two classical models describing the current flowing through such a barrier – the Bethe theory, which assumes large depletion region with respect to the mean free path and assumes the drift diffusion limitations as the bottleneck of the process. The Schottky theory, just the contrary, assumes that all the electrons moving towards the metal with high enough energy, cross the barrier, thus the transport process is emission limited.

For the first case the macroscopic continuity equation can be expressed in the form: $J_n = q(\mu_n nE + D_n \frac{dn}{dx})$,

where J_n is the current density, n is the carrier concentration, E is the electric field strength, μ_n is the carrier mobility and D_n is the diffusion coefficient. The equation can be used to express the current if the electrostatic potential and the carrier concentration are given as a function of the applied voltage, which is achieved by solving the Poisson equation:

$$\frac{d^2\phi}{dx^2} = -\frac{\rho}{\varepsilon_s} = -\frac{q}{\varepsilon_s}(p - n + N_d^+ - N_a^-),$$

where ϕ is the electric field potential, p is the holes concentration, N_d^+ and N_a^- are the concentrations of the ionised donors and acceptors, respectively. This differential equation cannot be solved analytically, without certain assumptions, the simplest one of which is the full depletion approximation – the donors are considered fully ionised in the region close to the interface with the metal of width:

$x_d = \sqrt{\frac{2\varepsilon_s(\phi_i - V_a)}{qN_d}}$, for an applied voltage V_a. The barrier height and the build-in potential given, respectively, by $\phi_B = \Phi_M - \chi$ and $\phi_i = \phi_B - \frac{kT}{q}\ln\frac{N_c}{N_d}$. The current density can thus be expressed like:

$$J_n = \frac{qD_n N_c}{kT}\sqrt{\frac{2q(\phi_i - V_a)}{\varepsilon_s}}\exp(-\frac{q\phi_B}{kT})[\exp(\frac{qV_a}{kT})-1].$$

Alternatively, as required in the second model, the current density may be calculated estimating the number of electrons with high enough energies to go over the barrier like:

$J_n = \int_{E_c(x=+\infty)}^{q\phi_n} qv_x \frac{dn}{dE}dE$. A simple, yet, unnecessary detailed calculation leads to the result:

$$J_n = \frac{4\pi q m^* k^2}{h^3}T^2\exp(-\frac{q\phi_B}{kT})[\exp(\frac{qV_a}{kT})-1].$$

For thin enough barriers, at low temperature, and in reversed bias, another contribution may become important – the tunneling current. Given the barrier shape the current can be estimated by solving the Schrödinger equation:

$-\frac{\hbar^2}{2m^*}\frac{d^2\Psi}{dx^2} + V(x)\Psi = E\Psi$, with mixed boundary conditions at infinity, yielding:

$$J_n = qv_R n\exp(-\frac{4}{3}\frac{\sqrt{2qm^*}}{\hbar}\frac{\phi_B}{E}).$$

From the minor current components, one important contribution is created by the recombination in the depleted region. This process can be considered as a direct transition through the band-gap. The current density can be estimated like:

$J_n = \frac{qn_i l}{\tau}\exp(\frac{qV_a}{2kT})$, and is likely to be relatively more important in high barriers, in materials of low carrier lifetime, at low temperature and at low bias voltage. It is a common cause of error as it changes the effective activation energy, measured in the temperature dependencies.

The minority carrier currents are inversely proportional to the appropriate barrier heights: $J_p \propto \exp(-\frac{\phi_p}{kT})$ and $J_n \propto \exp(-\frac{\phi_b}{kT})$, where $\phi_p = E_g - \xi$ and ζ is the energy of the donors with respect of the bottom of the conductance band in the semiconductor. Along with the dominant current due to the electrons, there is a small flux of injected holes, the injection ratio: $\frac{J_p}{J_n} = \gamma \propto \exp(-\frac{(\phi_p - \phi_b)}{kT})$ is normally much less than unity. The injection ratio in not a constant and above certain current density grows linearly with the current. The injection ratio is further increased in the presence of a thin insulating layer at the metal-semiconductor interface. The presence of this layer may be modeled as a thin tunnel barrier between the metal and the semiconductor, taking part of the total voltage drop, thus decreasing the actual applied voltage on the Schottky barrier itself. In rigid zones approximation this is visualized on Fig. 2-2.

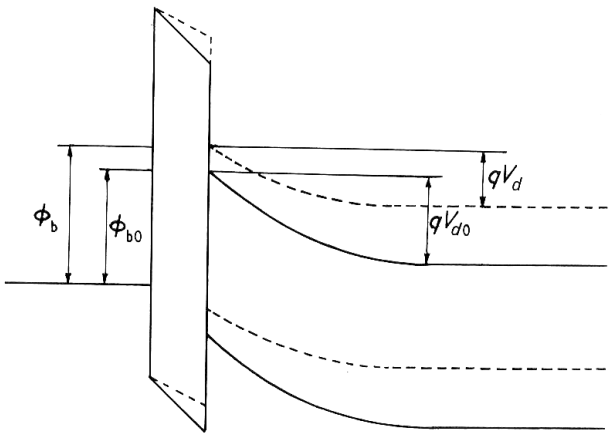

Figure 2-2 Influence of a insulating layer at the interface.

The current density in this case may be expressed like:

$$J_n = J_s \exp(q\frac{V_a - 2\Delta\phi\left[1-\sqrt{1+\frac{\phi_i - V_a}{\Delta\phi}}\right]}{kT}),$$

where the shift of the barrier potential is expressed as $\Delta\phi = \frac{qN_d d^2}{\varepsilon_s}\left(\frac{\varepsilon_s}{\varepsilon_{ox}}\right)^2$, ε_{ox} being the permeability of the oxide tunnel barrier. Because of the potential drop in the interfacial layer the barrier height is being lowered. The current density is reduced because of the additional barrier by an amount nearly proportional to $\Delta\phi$.

Another detrimental effect is the lowering of the barrier height, due to image charges in the metal. The resulting change may be estimated like: $\Delta\phi_b = \sqrt{\frac{qE_{\max}}{4\pi\varepsilon_s}}$, where $E_{\max}$ is the maximal electric field strength in the interface region.

As a first order approximation the effect of an external magnetic field on the junction may be considered as effective change of the barrier height due to the Zeeman splitting of the quasi-Fermi level in the metal.[2] In the thermo-ionic emission model this can be described introducing spin-polarized currents:

$$J_{\updownarrow} = q\int_{E_c}^{q\phi_n} v_{\text{F}\updownarrow}\frac{dn_{\updownarrow}}{dE}dE,$$

which when the energy of the excitations is not too large may be approximated by the energy averages (at the quasi-Fermi level) as $J_{\updownarrow} = q\left\langle v_{\text{F}\updownarrow} n_{\updownarrow}\right\rangle_{E_{\text{F}}}(q\phi_n - E_c \pm g\mu_{\text{B}}B)$. The magneto-conductance ratio:

$$MC = \frac{(J_{\uparrow B} + J_{\downarrow B}) - (J_{\uparrow 0} + J_{\downarrow 0})}{(J_{\uparrow 0} + J_{\downarrow 0})},$$

can be thus approximated, for the case of small fields, with:

$$-\frac{\langle v_F n_\uparrow\rangle - \langle v_F n_\downarrow\rangle}{\langle v_F n_\uparrow\rangle + \langle v_F n_\downarrow\rangle}\frac{g\mu_B B}{kT} \approx -\alpha_c \frac{g\mu_B B}{kT}.$$

As is it is easily noticed, the effect is small, of the order of 1 per cent in 5 T (easily achievable field with a superconducting magnet) and room temperature.

For the case of drift-diffusion limited transport, the derivation of the magneto-conductance ratio is more involved and features completely new behavior, namely the effect is non-zero even when the metal is completely spin-symmetric:

$$MC \approx \frac{D_\uparrow\sqrt{\frac{2q}{\varepsilon_s}(\phi_B - g\mu_B B) + const} + D_\downarrow\sqrt{\frac{2q}{\varepsilon_s}(\phi_B + g\mu_B B) + const} - \left(D_\uparrow\sqrt{\frac{2q}{\varepsilon_s}\phi_B + const} + D_\downarrow\sqrt{\frac{2q}{\varepsilon_s}\phi_B + const}\right)}{D_\uparrow\sqrt{\frac{2q}{\varepsilon_s}\phi_B + const} + D_\downarrow\sqrt{\frac{2q}{\varepsilon_s}\phi_B + const}}$$

where $D_\updownarrow$ is the spin-dependent diffusion coefficient. This effect is a kinetic analog to the week Pauli paramagnetism of the quasi-free gas in nonmagnetic metals.

The exact sense of the averaging operations in the above expressions for MC is dependent upon the excitation mechanism (normally thermal activation over the barrier or alternatively photo activation, when the junction is irradiated by external light source).

2.2 Magnetism of Carbon

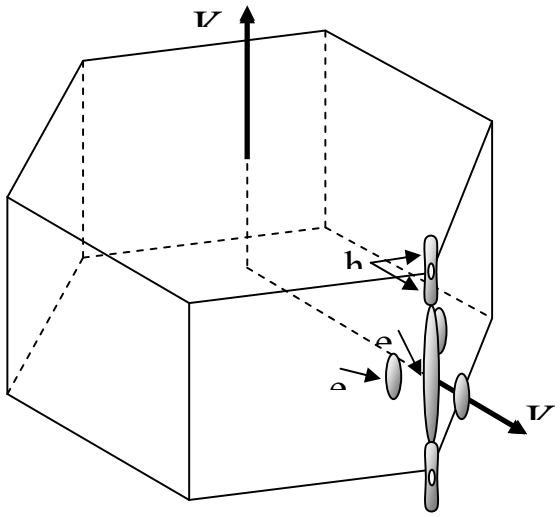

The magnetic properties of graphite and other structures composed of graphene-like sheets are a subject of renewed scrutiny, following reports of ferromagnetism [3] and even superconductivity [4] in some of these carbon materials. It is difficult to be sure that small ferromagnetic moments are intrinsic effects in view of the ubiquity of low-level contamination of samples and addenda by traces of ferromagnetic iron or magnetite. There is also evidence, that magnetism can be induced by spin-polarized charge transfer at the interface between a ferromagnetic metal and carbon nanotubes [5] or a graphite sheet[6].

Carbon-based solids are normally diamagnetic. The main contribution is orbital diamagnetism from electrons confined in closed orbits, including the inner electron shells: $\kappa_{orb} = -N\mu_0 e^2 \langle r_i^2\rangle / 6m_e$, where N is the number of atoms per unit volume, e and m_e are the charge and mass of the electron and $\mu_0 = 4\pi\ 10^{-7}$ T m A^{-1} is the magnetic constant. $\langle r^2_i\rangle$ is the mean square radius of the orbit in the xy plane, perpendicular to the applied field direction z. κ is the dimensionless SI susceptibility, which cannot exceed –1. For most solid elements it is in the range $-10^{-5} - 10^{-6}$. Diamond has $\kappa = -2.2\cdot 10^{-5}$. Compounds with benzene rings exhibit stronger diamagnetism because the π-electrons are confined in larger orbits. This helps to explain why the susceptibility of graphite is so anisotropic, with a value of -2.6 10^{-4} when the field is applied along the c-axis, but the in-plane susceptibility, -3.8 10^{-6}, is less than that of diamond.

Further contributions to the susceptibility arise from the conduction electrons. In a magnetic field, the electronic energy levels condense into a few, highly degenerate Landau levels. The Landau diamagnetism for the free-electron gas $\kappa_L = -N\mu_0\mu_B^2/2kT_F$ is precisely one third as large as the Pauli paramagnetic susceptibility κ_P, but of opposite sign [7]. Here T_F is the Fermi temperature, and N_e is the conduction electron density. More generally, the ratio κ_L/κ_P is $(1/3)(m_e/m^*)^2$, because the Landau term depends on the effective mass m^*. When m^* is small, the diamagnetic contribution can outweigh the paramagnetic one. As the Landau levels are swept through the Fermi level, characteristic de Haas - van Alphen (dHvA) oscillations appear in the low temperature susceptibility.

The electronic structure of nanotubes depends on their radius and chirality. A tube is represented by a pair of integers (n, m) or the chiral vector **L** = n**a** + m**b**, along which the tube is wound from the graphene sheet. Imposing periodic boundary conditions in this form, the structure can be calculated by means of a tight-binding model and the band structure of a 2D graphene sheet. A **k.p** method or effective mass approximation is also successful in describing a variety of electronic properties, including the Aharonov – Bohm effect [8] and the bulk value of the diamagnetic susceptibility of ensembles of nanotubes [9].

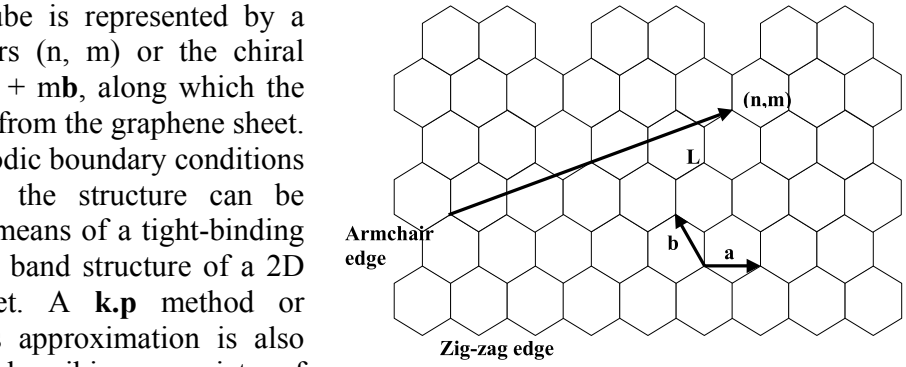

The bulk magnetic susceptibility has not been measured for single-walled specimens for a specific n and m. Single-walled nanotubes are grown using a transition-metal catalyst which forms a particle at the end of the tube. The ferromagnetic signal from these iron or cobalt particles may obscure the response of the tube itself. The orbital moment may, though, be deduced from the conductance through a gated nanotube in an applied magnetic field. The values of the orbital moment are estimated to be 10-20 Bohr magnetons. [10]

Data are available, however, for multi-walled tubes which are mixtures of tubes of different radii and chirality. [11], [12] The anisotropy of the susceptibility and the spin gyro-magnetic ratio was studied on partially oriented ensembles [13] and the temperature dependence of the perpendicular component of the magnetic susceptibility is explained in terms of a simple two band electronic structure. [14] The analysis of the existing data on magnetisation of ensembles of nanotubes is complicated by the following factors.

a) The magnetisation of the ensemble is generally non-linear with field (which may be due to ferromagnetic impurities at small fields, or intrinsic, due to size effects in the tubes at high fields).

b) The anisotropy of the magnetisation has to be inferred from partially oriented samples.

c) The magnetisation exhibits substantial temperature dependence, which may be different for different partial orientations.

d) It is difficult to acquire substantial amounts of ultra-high purity nanotubes.

3 Description of Research

3.1 Magnetic and Nonmagnetic Schottky junctions

3.1.1 Practical Considerations on the Passive and Active Transport Characteristics of Schottky junctions

Even though the basic idea behind a spin-polarization measurement using Schottky junction is quite simple, there are few practical limitations that have to be considered:

a) Any active current flowing through the junction inevitably produces resistance drop on the substrate, which often has high magnetoresistance. The resulting problem is intrinsically non-linear. It is therefore necessary to measure at low applied bias voltages, and suffer from signal/noise ratio.

b) The barrier resistance, as well as the substrate resistance often depend exponentially on temperature, which should be kept constant to within 0.1 %.

c) In a photovoltaic measurement, apart from the dominant effect of the internal photoemission of electrons from the metal to the semiconductor, if the light is not well low-pass filtered, there is a contribution of direct-gap excitations in the depleted region of the semiconductor.

3.1.2 Transport Measurements on Schottky junctions

A very important step in characterising the Schottky diode structures is the estimation of the series resistance contribution (the resistance of the participating in the active transport part of the semiconductor substrate) and the linearity of the non-rectifying back contact. An example of indium-alloyed contact on n-type silicon is given on Fig. 3-1.

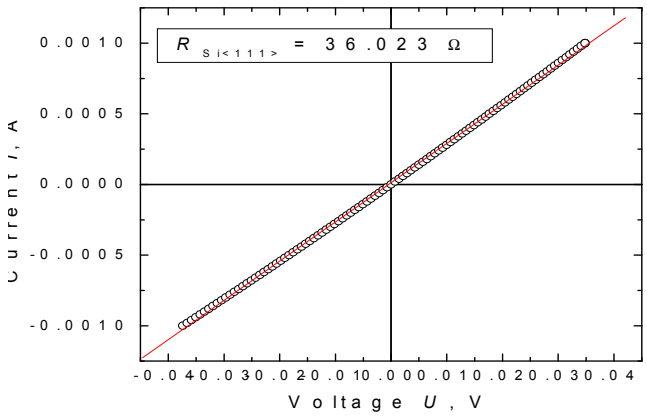

Figure 3-1 Current-voltage characteristic of a Ohmic back contact to Si.

The series resistance due to the semiconductor substrate has a substantial influence on the current-voltage characteristics of the Schottky diodes, especially at high currents and low temperatures. Because of the voltage drop on the substrate, the bias on the junctions is different from the measured one by an amount that is non-linear in

applied voltage and magnetic field. Observation of small effects due to intrinsic magnetoresistance effects in the barrier region is readily obscured by large series resistance and magnetoresistance. The magnetoresistance ratio can be as high as 25 % in 5 T at 300 K for medium n-doped Si, see Fig. 3-2, and about 5 % in 5 T for GaAs.

When a large amount of diodes have to be fabricated, it is important, that their rough characterisation is a fast timesaving process. An example of such a measurement, using a fast alternating current and voltage hysteresiograph is shown on Fig. 3-3. This technique allows, also, for the estimation of the junction capacitance and breakdown voltage.

A simple, but not free from artefacts, method for observation of the current-voltage characteristic of any non-linear device is the direct current (voltage) source – volt (ampere) meter. A current source is to be preferred at high impedances and because of the lower noise levels that can be achieved. On Fig. 3-4 the different character of the magnetic and non-magnetic junctions is easily seen. The reason for the current saturation however is due to the drift-diffusion limitation in some of the junctions, and not due to the ferromagnetic character of the corresponding metals. These substantial differences in the dominant transport mechanism necessitate the use of both the thermo-ionic emission model and the drift-diffusion model for data analysis.

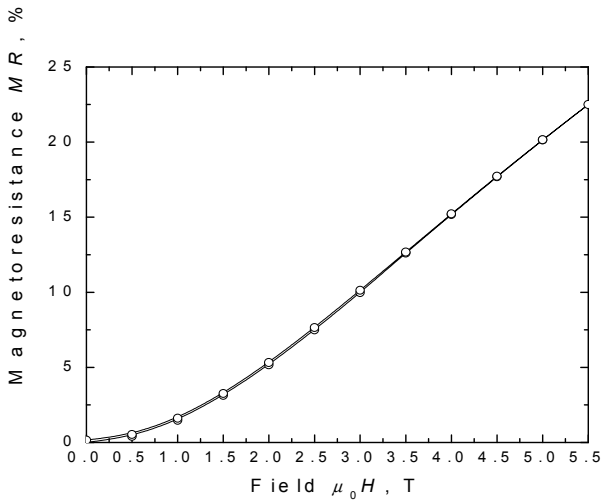

Figure 3-2 Magnetoresistance of n-type Si substrate at 300K.

For the measurement of the field dependence of the current-voltage characteristics, a method with a much better signal-noise ratio and stability may be applied, namely, measurement of the AC differential conductance at an arbitrary DC bias and consecutive numerical integration. The resulting reconstructed diode characteristics have significantly smaller errors in the small bias region, which facilitates the eventual resolution of small effects due to the application of external magnetic field. On Fig. 3-5 and 3-6, two illustrative examples for the cases of CoFe and Cu on Si, are presented. The observed magnetic-field-induced changes are, however too big to be attributed the Zeeman splitting effect described in Chapter 2. It is easily noticed that the effect is more

pronounced at high DC biases, or when the current is high, which is in favor of magnetoresistance contribution of the semiconductor substrate.

A further improvement of the measurement technique is making direct difference between the differential conductance of two diodes one inside the region of the applied magnetic field, sharing the same isothermal bath. By this method taking advantage of excellent temperature stabilization and noise cancellation, differences as small as 10^{-5} are easily resolved. Results for Cu, Co and CoFe junctions on n-type Si are shown on Fig. 3-7, 3-8, 3-9, respectively. A closer look at the Co and CoFe differences reveals a crossover point around 1-2 V, positive bias, that is attributed to the transition between thermo-ionic emission limitation on the current transport over the barrier to the drift-diffusion limited case. The maximal possible value of the effect of 2.5 % at 5 T and 300 K under the thermo-ionic emission model is exceeded in all cases, either in positive or negative bias. This fact one more time reinforces the role played by the drift-diffusion limitations for the active transport through Schottky diodes at room temperature.

The harshness of the problem with the series resistance can be further illustrated by the strong magnetic field dependence of the reverse bias resistance of the junctions, as illustrated on Fig. 3-10. It is easily seen that at high negative potentials, there is a competition between the junction breakdown process and the magnetoresistance of the substrate (combined with heating effects at very high currents).

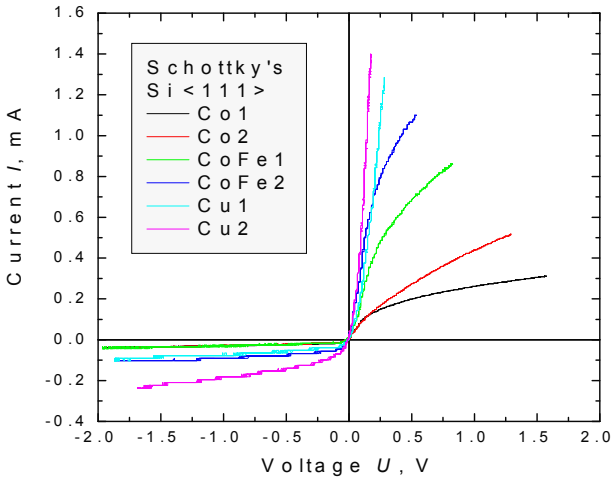

Figure 3-3 Current-voltage characteristics of set of Schottky junctions.

To recapitulate, due to numerous side effects the measurement of spin-polarization, using active transport through Schottky junctions impossible for the most common metal-semiconductor systems. While there is no general solution for the problem, it may be possible to measure polarization using this method at particular set of circumstances, namely, low Schottky barrier height and compliance to the thermo-ionic emission model at low temperatures.

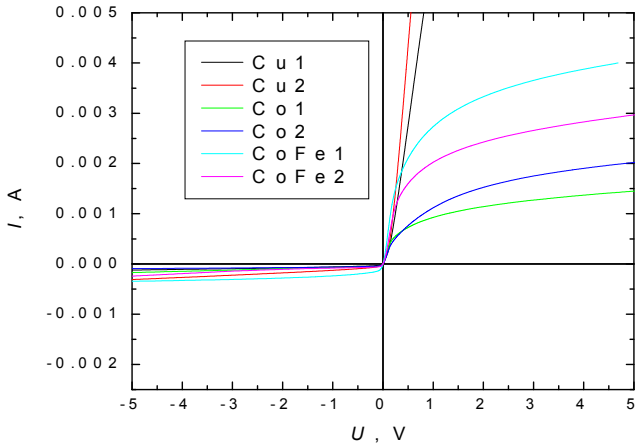

Figure 3-4 Set of current voltage characteristics measured with a source-meter.

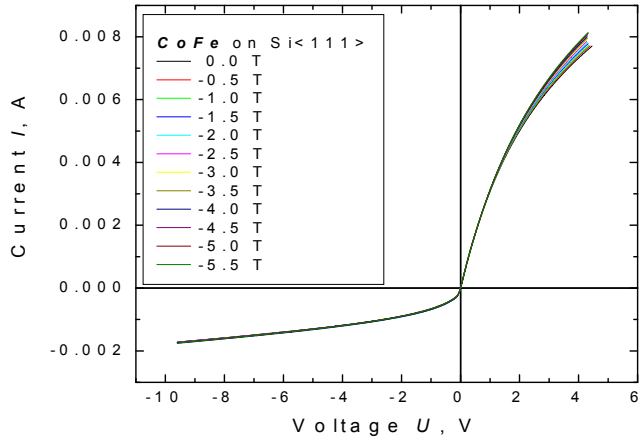

Figure 3-5 Set of reconstructed current-voltage characteristics at 300 K.

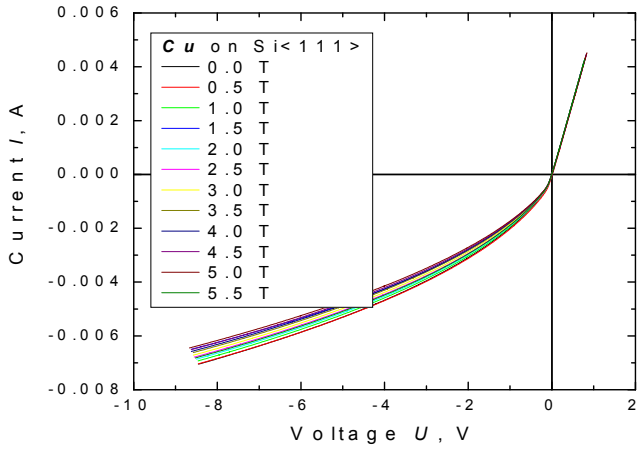

Figure 3-6 Set of reconstructed current-voltage characteristics at 300 K.

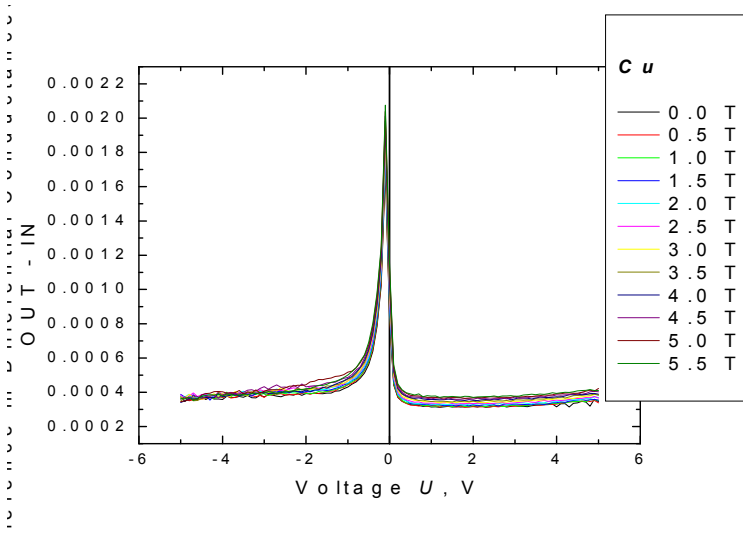

Figure 3-7 Differential one-in/one-out measurement of the differential conductance.

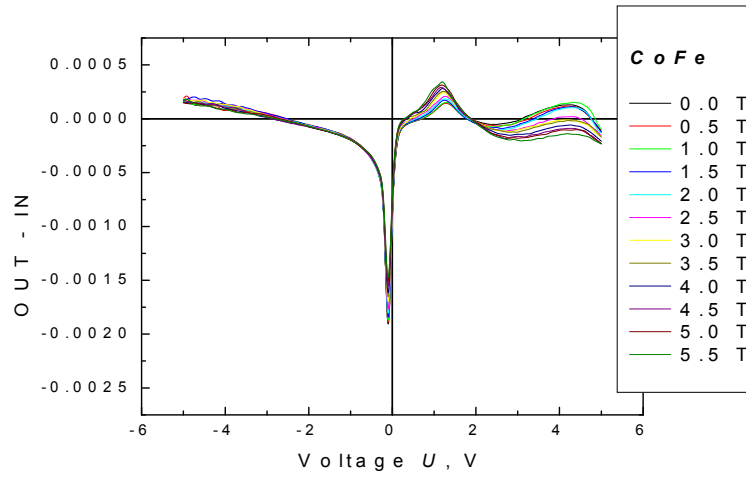

Figure 3-8 Differential measurement one-in/one-out of the differential conductance.

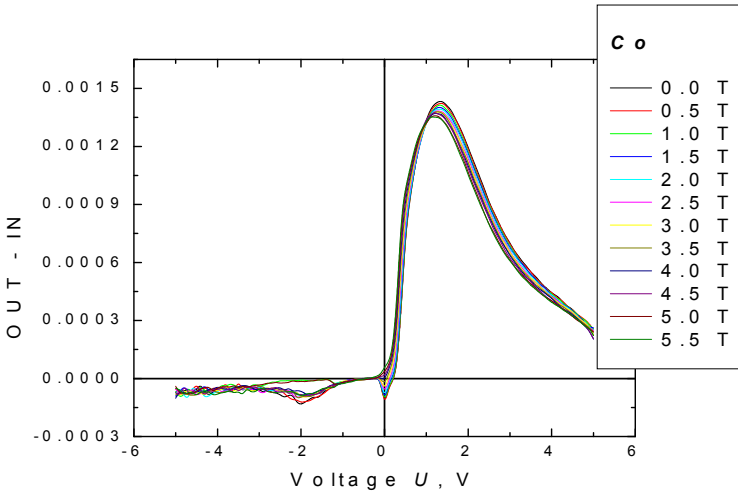

Figure 3-9 Differential measurement one-in/one-out of the differential conductance.

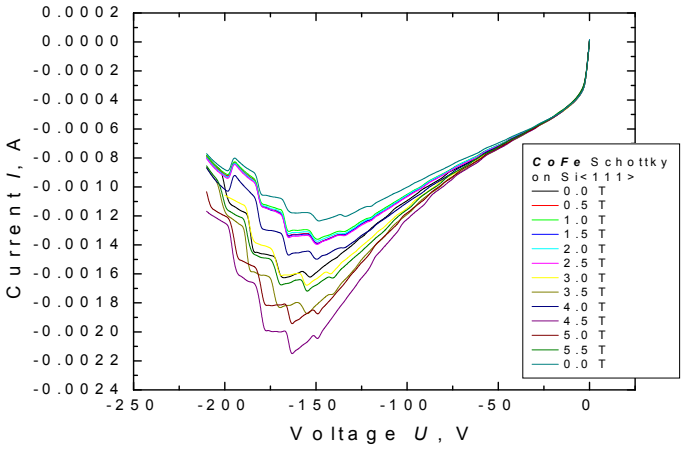

Figure 3-10 Reverse bias breakdown at 300 K.

3.1.3 Magneto-Optical Measurements on Schottky junctions

A simple way to avoid large contributions from the magnetoresistance of the semiconductor substrate is to substitute the active current measurements with photovoltaic or photo-galvanic ones. For the case of the photovoltaic method of determination of changes in the barrier height, the measurement is essentially electrostatic as the photocurrent is compensating the drift-current within the depleted region in the semiconductor. Quite the opposite way photo-galvanic measurement is almost exactly short-circuit measurement, so the bias on Schottky barrier tends to zero, and therefore the virtual voltage drop is predominantly on the barrier, as its resistance tends to the tunnelling limit.

Simple way to characterize the dependency of the photo-voltage on the light illumination (with continuous spectrum) is shown on Fig. 3-11. Different thickness of white absorber is placed between the light source and the junction. As the illumination depends exponentially on the absorber thickness, the actual relation photo-voltage vs. illumination may be deduced. For a large range of fluencies that is a linear relationship.

In order to determine the spin polarisation around the quasi-Fermi level at a given temperature, the change of the photo-voltage or the photocurrent with applied magnetic field, under constant illumination may be investigated. Results for different ferromagnetic and non-magnetic metals deposited on n-type Si and GaAs are shown on Fig. 3-12, 3-13 and 3-14. It is impossible to account for the observed effects of few percent in 5.5 T in the framework of the thermo-ionic emission model. As the large shifts of the photo voltage are not accompanied by corresponding change of the short-circuit current, the influence of the bulk magnetoresistance of the substrate can be excluded as a factor. A reasonable explanation may be found only in the drift-diffusion limit, but whether the change in photo-voltage may be attributed to a change of the barrier height, or simply due to different diffusion coefficients for spin-up and spin-down electrons, remains an open question. The fact that all the shifts observed on GaAs substrates are

within the experimental uncertainty of 0.1 % is related to the well-known fact that the Schottky barrier height at the metal to GaAs interface is determined predominantly by interface states and not by the difference of the work-functions.

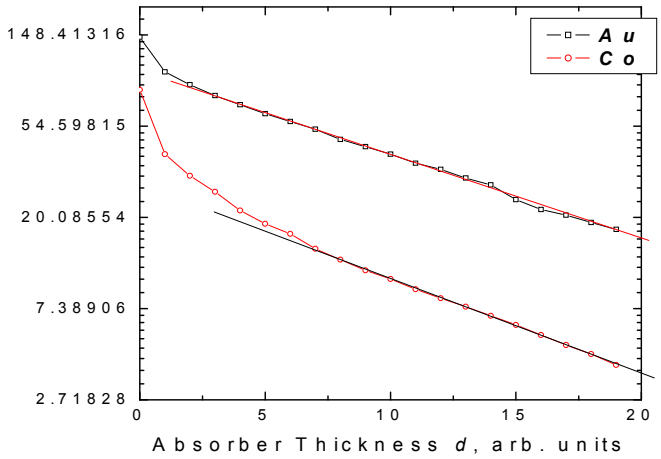

Figure 3-11 Illumination calibration of the open-circuit photo-voltage.

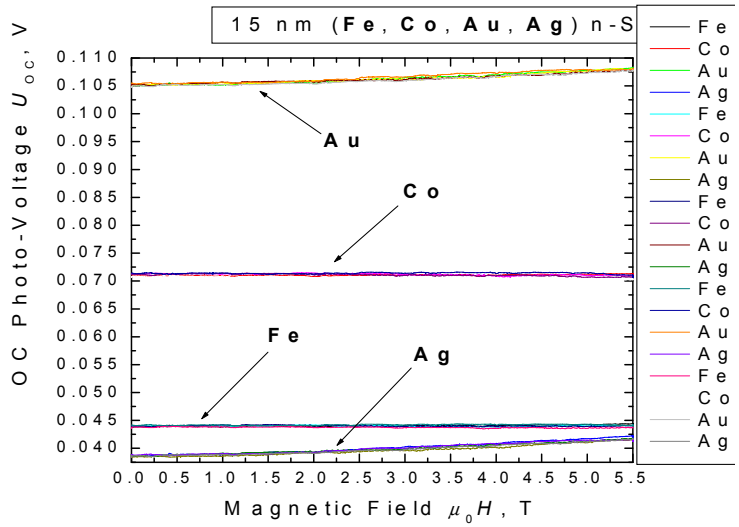

Figure 3-12 Open circuit photo-voltage vs. applied field at 300 K.

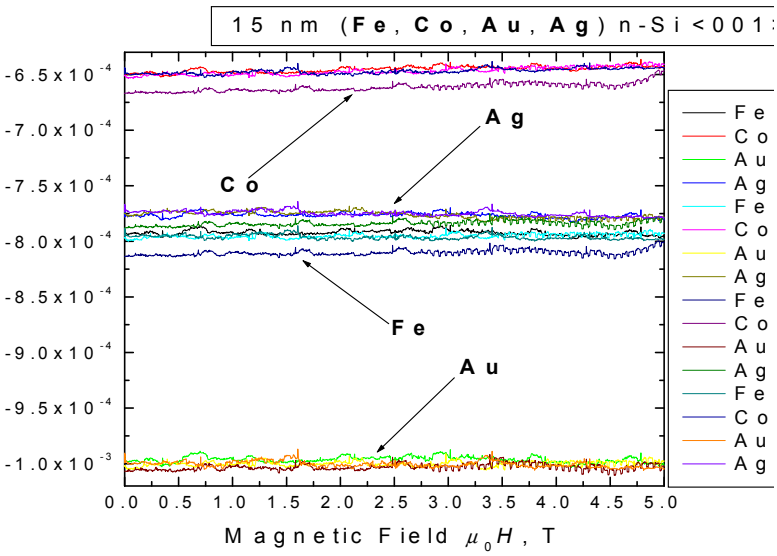

Figure 3-13 Short circuit photo-current vs. applied field at 300 K.

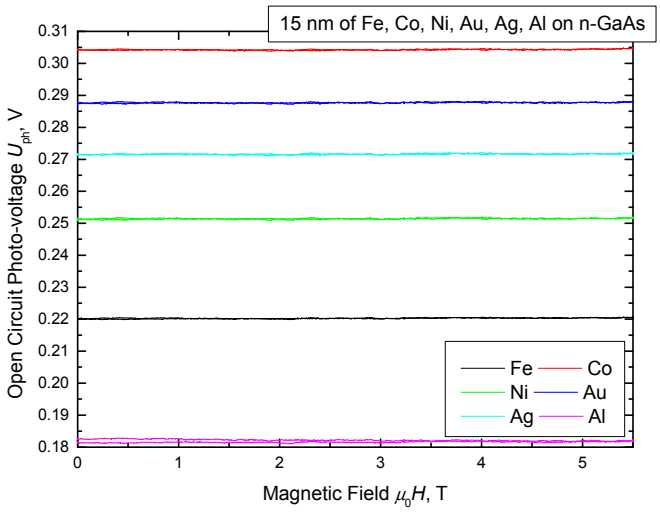

Figure 3-14 Short circuit photo voltage vs. applied field at 300 K.

3.1.4 Conclusions on the Plausibility of Spin Polarisation Measurements Using Schottky Diodes

While direct active transport measurement of the spin-polarisation is generally unrealisable, there may be a particular system metal-semiconductor, where all of the following requirements are satisfied:

a) The magnetoresistance in the bulk-semiconductor is small and preferably linear, even in fields of 5 – 10 T.

b) Low Schottky barrier height, so that the measurement can be performed at low temperatures.
c) The substrate should be still conductive at the lowest temperature of operation of the junction, and have small temperature dependence of the resistivity.
d) The junction complies sufficiently well with the thermo-ionic emission model, and does not include a thin oxide interfacial layer.
e) The Schottky barrier height should be determined by the difference of the work functions of the two materials in the junction and not by interface pinning.

The conditions that must be satisfied for a successful photovoltaic measurement of the spin-polarization are as follows:

a) The Schottky barrier height should be sufficiently different from the band gap of the semiconductor, as to avail for the separation of the internal photoemission and the direct gap contributions by experiment.
b) The metal layer has to be sufficiently transparent at the frequencies of interest, and in the same time sufficiently thick to preserve bulk behavior.
c) The temperature dependence of the Schottky barrier height should be sufficiently small.
d) The Schottky barrier height should be determined by the difference of the work functions of the two materials in the junction and not by interface pinning.

3.2 HOPG and MW Carbon Nanotubes

3.2.1 Diamagnetism of Graphite

In order to check the speculations about room temperature ferromagnetism in graphite, as described in the introduction, several samples of different grades HOPG were examined. Representative results are shown at Fig. 3-15. Only one of eight samples shows any saturating component of the magnetisation at 300 K. This fact leads to the conclusion that the effects are most likely spurious and due to low-level contamination.

The magnetisation when the field is applied parallel to the *c* axis is predominantly linear. The characteristic for the quasi-free electron gas de Haas van Alphen oscillations can be sensed at low temperature as demonstrated on Fig. 3-16. The in-plane susceptibility is much smaller, as shown on Fig. 3-17, and therefore a very small saturating component can be resolved. The fact that such behaviour is not present at high temperatures leads to two possible explanations. Either the trace impurities are becoming ferromagnetic at very low temperature (which is not expected for the most common impurity - Fe) , or paramagnetic moment due to loose spins concentrated on defects of the crystalline structure is saturating, following the Langevin function, at low temperatures and high magnetic fields.

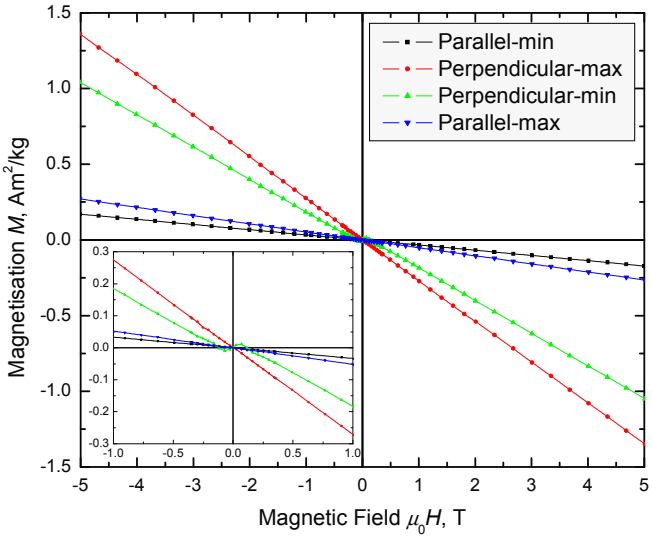

Figure 3-15 Magnetisation of HOPG at 300 K.

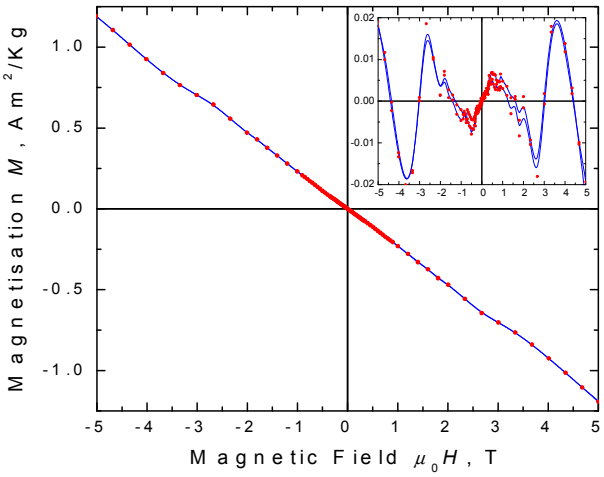

Figure 3-16 Magnetisation of HOPG at 1.8 K, with the field parallel to *c*.

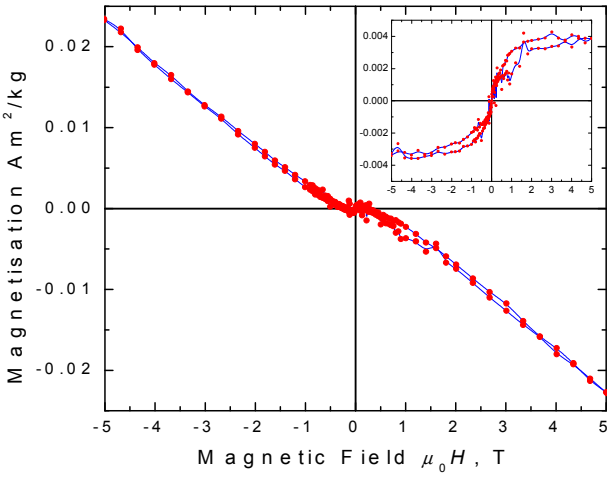

Figure 3-17 Magnetization of HOPG at 1.8 K, with the field perpendicular to *c*.

3.2.2 Oscillatory Kinetic and Thermodynamic Effects

A perfect illustration of the semi-metallic character of graphite is its enormous magnetoresistance at low temperature (the effects exceed 2000 %), as shown on Fig. 3-18. Below about 50 K the quasi-free electron gas exhibits explicit Landau quantization, with Hall oscillations amounting for about 30 % of the total signal at 5 T (Fig. 3-19).

When the direction of the applied magnetic field is in the plane of the graphene sheets, no oscillations can be observed, either in resistance or the Hall effect (Fig. 3-20, 3-21). The magnetoresistance is still substantial at low temperatures, but the effect may be due to misalignment (the conductivity tensor anisotropy reaches about 100:1).

In the longitudinal magnetoresistance and Hall contribution, very long period oscillations can be observed (Fig. 3-22, 3-23) on the account of the large anisotropy of the Fermi surface, about 25:1 for the majority electron component, and 17:1 for the majority hole component.

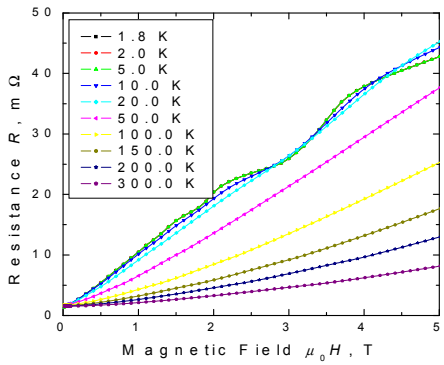

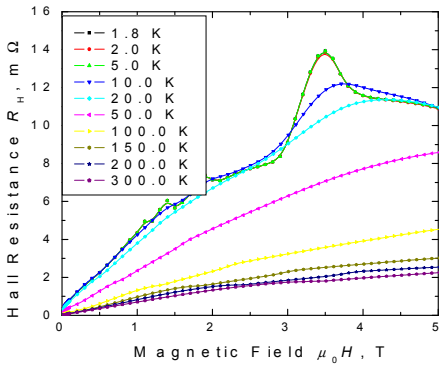

Figure 3-18 Resistance at different temperatures with field along *c*. (left)

Figure 3-19 Hall resistance at different temperatures with field along *c*. (right)

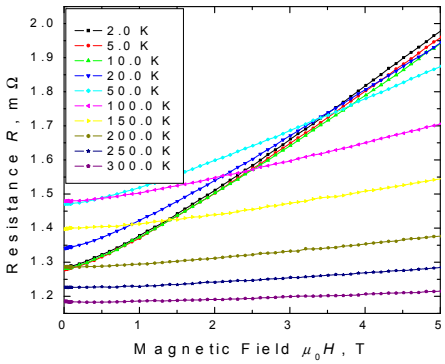

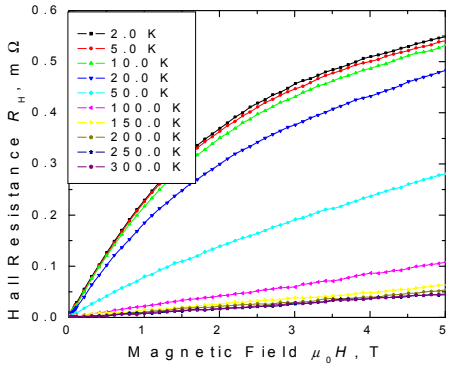

Figure 3-20 Resistance at different temperatures with the field perpendicular to *c*. (left)

Figure 3-21 Hall effect at different temperatures with the field perpendicular to *c*. (right)

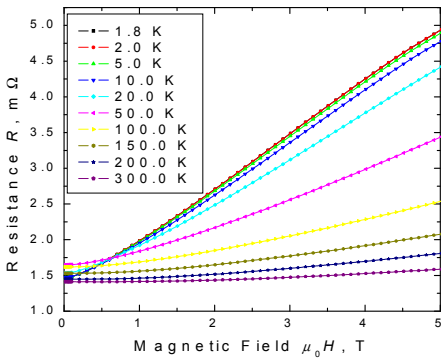

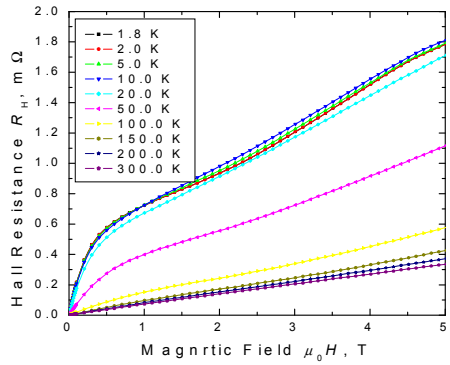

Figure 3-22 Longitudinal magnetoresistance with the field perpendicular to *c*. (left)

Figure 3-23 Hall effect contribution with the field parallel to the current. (right)

Possible metal-semiconductor transition is revealed on Fig. 3-24 for fields as low as 0.1 T. A dramatic decrease in carrier concentration is evidenced by the enormous increase of the hall resistance (see Fig. 3-25). When the field is applied in the plane of the graphene sheets the effect is far less pronounced both in the resistance and Hall effect dependencies on temperature (see Fig. 3-26, 3-27). It becomes evident, what is speculated to be re-entrance in metallic state at very-low temperatures (field dependent series of metal-to-insulator-to metal transitions) is likely to be related to the large amplitude of the Shubnikov de Haas oscillations, due to the very small effective mass (less than 0.04 m_e).

The picture of a very anisotropic quasi-free electronic system remains valid remains valid down to 0.3 K and as high as 23 T, as evidenced on Fig. 2-28. The magnetoresistance does not saturate in any orientation, neither shows very close to parabolic dependence on field, therefore, truly open or completely closed electron orbits if any, would not evolve the majority carriers.

A much more detailed analysis of the oscillations of the kinetic coefficients, suggested by Landau [7], may be performed as shown on the series of figures (3-29 to 3-

34). The results for the various quasi-particles may be summarized in the following list and compared to the appropriate references:

1. 0.33 T – minority h (0.34 T – Williamson; 0.32 T – Luk'yanchuk)
2. 0.50 T – minority e (0.74 T – Soule; 0.75 T – Anderson)
3. 1.28 T – minority h (0.9 T – Woolam; 1.17 T – Flood)
4. 4.17 T – majority e (4.8 T – Soule; 4.7 T – Cooper)
5. 6.06 T – majority h (6.2 T – Woolam; 6.06 T – Cooper)
6. 10.9 T, 14.3 T, 18.2 T, 26.3 T – e + h (breakthrough).

I. A. Luk'yanchuk, Y. Kopelevich, arXiv:cond-mat\0402058 (2004)
J. A. Woolam, Phys. Rev. B, **3**, 1148 (1971); Phys. Rev. **4**, 3393 (1971)
J. D. Cooper, J. P. Smith, at. al., J. Phys. C: Solid St. Phys. **4**, 442 (1970)
D. J. Flood, Phys. Letters, **30A**, 168 (1969)
J. R. Anderson, W. J. O'Sullivan, at. al., Phys. Rev. **164**, 1038 (1967)
S. J. Williamson, S. Fouler, M. S. Dresselhaus, Phys. Rev. **140**, A1429 (1965)
D. E. Soule, J. W. McClure, at. al., Phys. Rev., **134**, A453 (1964)

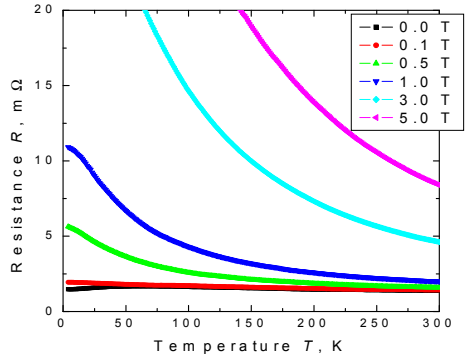

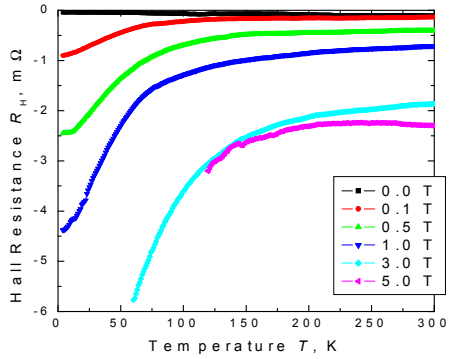

Figure 3-24 Resistance as a function of temperature at different fields applied parallel to the *c*. (left)

Figure 3-25 Hall effect as a function of temperature at different fields. (right)

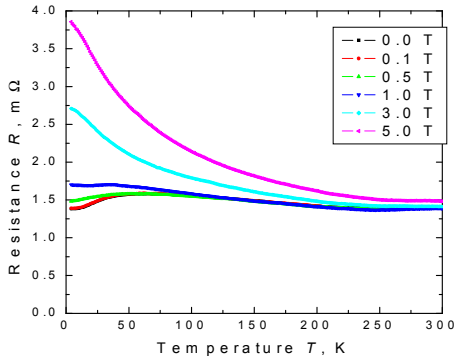

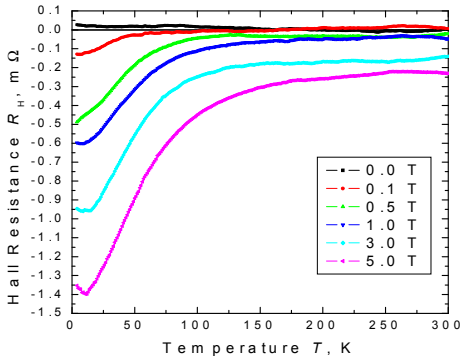

Figure 3-26 Resistance as a function of temperature at different fields applied perp. to *c*. (left)

Figure 3-27 Hall contribution as a function of temperature at fields applied perp. to *c*. (right)

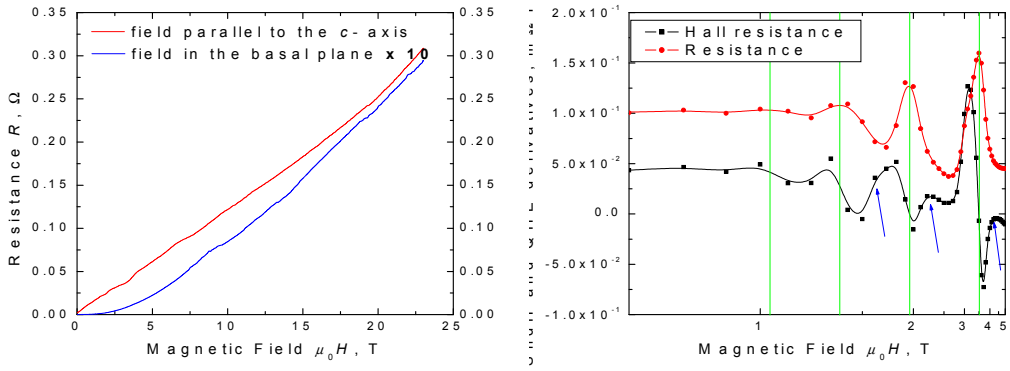

Figure 3-28 Resistance as function of the applied field of up to 23 T. (left)

Figure 3-29 Oscillations of the conductivity at 1.8 K. (right)

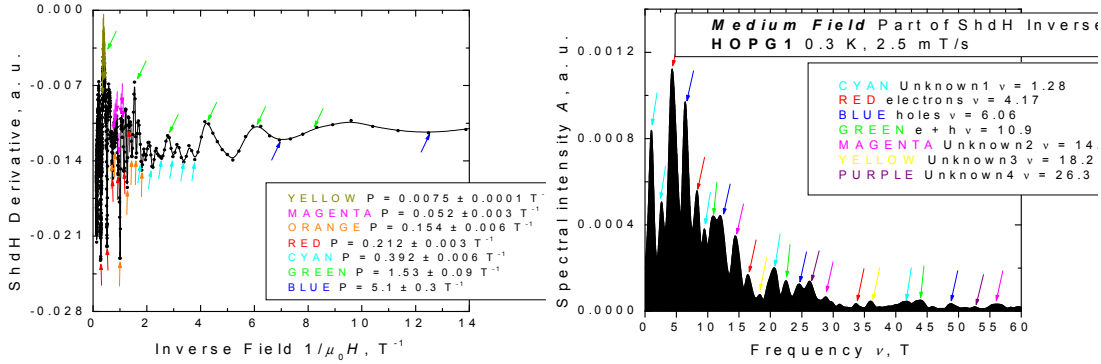

Figure 3-30 Conductivity oscillations at 0.3 K. (left)

Figure 3-31 Inverse domain image of the ShdH oscillations. (right)

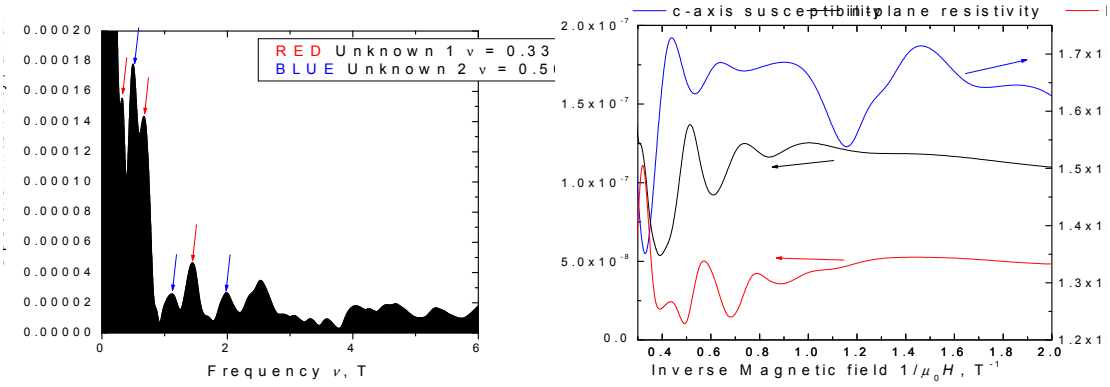

Figure 3-32 Low frequency components in the ShdH spectrum. (left)

Figure 3-33 Oscillations in the thermodynamic and the kinetic coefficients. (right)

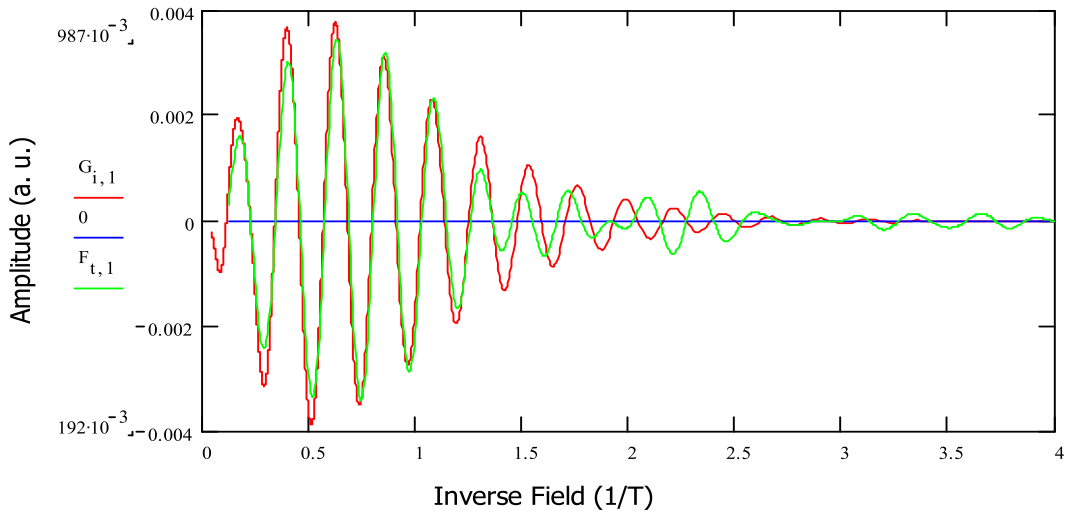

Figure 3-34 Band-pass filtered (3 – 5 T) majority electrons' component of the oscillatory conductivity GREEN and a fit using the L-K approximation RED, with parameters: T = 0.3 K, m^* = 0.039 m_e, T_D = 5 K, A_{ex} = 4.2 10^{16} m^{-2}, φ = -p/2

3.2.3 Theoretical Considerations on the Diamagnetism of Carbon Nanotubes

In the standard, the Schrödinger equations for an ensemble of N_e identical quasi-free electrons in a magnetic field along the z-axis of the system each has the form:

$$-\frac{\hbar^2}{2m^*}\nabla^2\Psi_j + i\frac{B_z e\hbar}{2m^*}(x_j\partial_{y_j} - y_j\partial_{x_j})\Psi_j +$$

$$+\frac{B_z^2 e^2}{8m^*}(x_j^2 + y_j^2)\Psi_j - sg_s^*\mu_B B_z\Psi_j = E\Psi_j \quad ,$$

which is equivalent to the Schrödinger equation for a harmonic oscillator, with eigenvalues given by:

$$E_{n,s} = \frac{\hbar^2 k_z^2}{2m_l^*} + g_t^*\mu_B B_z(n + \frac{1}{2}) - sg_s^*\mu_B B_z$$

where m_l^* and m_t^* are the longitudinal and transverse components of the effective mass tensor, and we have substituted $\hbar e/m_t^* = g_t^*\mu_B$. $n = 0,1,2\ldots$ is the Landau level index.

The electron gas is diamagnetic only if the effective mass of the carriers is small, in other words, when $g_t^* > g_s^*$. This is borne out by the small transverse effective mass for graphite, 0.04 m_e. The first term in the spectral equation represents the kinetic energy of translation along the z-axis, the second term represents a set of energy levels, whose degeneracy depends upon the radius of the cylinder within which the electrons are confined, and is given by $G = eB_zR^2/h = R^2/2l_B^2$, while the last term represents the Zeeman splitting of the spin-up and spin-down levels.

The degeneracy may be determined by imposing periodic boundary conditions with periods $(L_x a, L_y a)$ in the *xy* plane, where *a* is the lattice constant. The wave numbers are then quantized with $k_x = 2\pi\nu_x / L_x a$, $k_y = 2\pi\nu_y / L_y a$. Thus we have one degenerate state (Landau level with index *n*) per area $2\pi l_B^2$ of the graphene sheet [15]).

The effect of the magnetic field along the tube axis is to confine the quasi-free electrons in a parabolic potential. When $r_t >> l_B$, this is a good approximation. However the confinement in nanotubes is due to the structure of the tube itself. The potential in which the confined electrons move in the *xy* plane can be approximated for low-lying states by a parabola, which will give rise to equidistant excited levels. The resulting effective potential may be represented as: $U_{\text{eff}}(x) = (m_t^* / 2)(\omega_0^2 + \omega_c^2)x^2$ where ω_0 is the frequency determined by the zero field confinement in the tube, and $\omega_c = eB_z / m_t^*$ is the cyclotron frequency. In addition to the applied field **B** or vector potential $\mathbf{A}_H = (\hbar / e\lambda^2)[-y, x, 0]$, there is a constant effective field $B_0 = \hbar\omega_0 / g_t^* \mu_B$, or vector potential $\mathbf{A}_D = (\hbar / er_t^2)[-y, x, 0]$ representing the curvature of the graphene sheets [16]. In the case of nanotubes with r_t = 10 nm, B_0 = 7 T; the dHvA oscillations are suppressed when $B_z < B_0$.

Macroscopic quantities such as magnetization and susceptibility are independent of the spiral structure of the nanotubes [17]. Therefore, the basic response of the system may be calculated from thermodynamic averages based on the single-electron energy spectrum. Following [7], the partition function in the grand-canonical ensemble is

$$Z = N\prod_{n=0}^{\infty}\left(1 + e^{-\frac{E_n - \mu}{kT}}\right)^{G(B_Z)}.$$

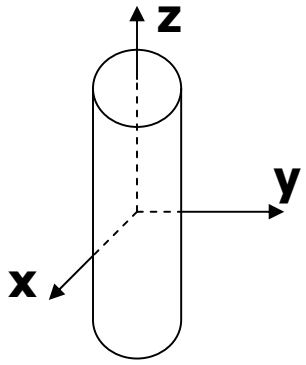

The chemical potential of the system, μ, is pinned between two Landau levels, and it can be considered fixed at $\mu = g_t^* \mu_B B(n_F + 1/2)$, where n_F is the number of completely filled levels (the Fermi level).

Considering the two levels, just below and just above the chemical potential, the grand canonical potential is

$$\Omega = -kT\ln(Z) = -NkT\ln\left(\prod_{n=n_F-1/2}^{n=n_F+1/2}(1 + e^{-\frac{E_n - \mu}{kT}})^{G(B_Z)}\right).$$

Furthermore, for electrons confined within a tube of radius smaller than l_B, corresponding to the maximum experimental field, the degeneracy $G(B_Z)$ can be considered a constant. The magnetization $M = -\partial\Omega / \partial B_Z$ and susceptibility $\kappa = \partial M / \partial B_z$ as a function of temperature and magnetic field oriented along the nanotube axis are therefore:

$$M(B_Z, T) = -Gg_t^* \mu_B N \tanh(g_t^* \mu_B B_Z / 2kT)$$
$$\kappa_L = -Gg_t^* \mu_B N(1 - \tanh^2(g_t^* \mu_B B_Z / 2kT)).$$

The total susceptibility is $\kappa_{tot} = \kappa_0 + \kappa_L(B,T)$ where the constant term κ_0 includes the Pauli, van Vleck and orbital diamagnetic contributions. However, the Landau levels will be broadened by thermal effects and by non-thermal scattering of the conduction electrons by defects, which are most simply represented by a Dingle temperature $T_D = \hbar / 2\pi k\tau_0$, where τ_0 is a relaxation time characterizing athermal scattering by defects $T \to T + T_D$.

The temperature-dependence of susceptibility when the field is applied perpendicular to the tubes has been described in the tight-binding approximation, where it is associated with the orbital diamagnetism of carriers in the 2D structure [14]. In order to model both the field and temperature dependence of the magnetisation, we associate the calculation of $\kappa_{||}$ in the confined-electron model with and a tight-binding calculation for $\kappa_{\perp}$. In the latter case, the magnetization perpendicular to the graphene sheet is

$$M(B_X,T) = -\frac{C\gamma_0^2 B_X}{(T+T_D)(2+\exp(\eta)+\exp(-\eta))},$$

where $\gamma_0 = 3$ eV is the 2D band parameter, η is the reduced Fermi level and $C = 5.45 \cdot 10\,\mathrm{Am^2/kgKT}$. η can be evaluated using the neutrality equation for the 2D graphite model $F_1(\eta) - F_1(-\eta) = (\eta_0^2/2)$, where $F_1(\eta)$ is the Fermi integral, T_0 is the degeneracy temperature of the carriers, $\eta_0 = T_0/(T+T_D)$ and the Dingle temperature remains remains a free. $\kappa_{\perp}$ is obtained from an average over the azimuthal angle, and the ensemble average κ is obtained form the average :

$$\tilde{M}(M_{||}(H),\chi_{\perp},H) = \int_0^{\pi/2} \sqrt{M_{||}(H\cos\alpha)^2 + (\chi_{\perp}H\sin\alpha)^2}\,\cos\left[\alpha - \arctan\left(\frac{\chi_{\perp}H\sin\alpha}{M_{||}(H\cos\alpha)}\right)\right]\sin\alpha\,\mathrm{d}\alpha$$

3.2.4 Experimental Results on MW Carbon Nanotubes

The magnetisation of macroscopic ensembles of carbon nanotubes exhibits a strongly non-linear magnetic field and temperature dependence, as illustrated on Fig. 3-30. The initial low-temperature susceptibility is twice larger than the high field and high frequency one. A detailed inspection of the raw data sets, see Fig. 3-31, reveals no artefacts from the measurement process. Correspondingly, the next step is to check whether the data can be fitted to the suggested in the previous chapter expression. Excellent fits are obtained, as demonstrated on Fig. 3-32.

A more detailed numerical calculation is visualized on Fig. 3-33, for both the perpendicular and parallel components of the magnetisation, as well as the ensemble average. All the important features of the experimental observations, compare with Fig. 3-34, are well reproduced.

An important next step is to compare the experimental data for the temperature dependence of the magnetisation in different fields, shown Fig. 3-35, with the theoretical predictions plotted on Fig. 3-36. There is a very good agreement, even without introducing corrections for the Van Vleck paramagnetic contributions.

The close correspondence of model and theory makes it possible to subtract the slowly varying contributions to the magnetisation, i. e. to do low-pass filtering of the data sets. The resulting curves reveal Landau susceptibility oscillations, which may be

compared to those measured in graphite on Fig. 3-37. Special attention should be paid to the largely different periods in the different orientations (related to the anisotropy of the Fermi surface) and the amplitudes of the oscillations, which are comparable for oriented nanotubes and HOPG, but trice smaller for the random ensemble of nanotubes. The latter fact strongly suggests that oscillations are only observed in the perpendicular component of the magnetisation.

In Fig. 3-38 we show the magnetoresistance of a compact of randomly oriented multi-walled nanotubes, which can be perfectly fitted to $R_{0T} - C \cdot M(H)^2$, as shown in Fig. 3-39, where C is a constant and M is the magnetization. The behavior may be attributed to powder magnetoresistance [18], where the tunneling from tube to tube is enhanced by the varied diamagnetic magnetization, which is coupled to the spin of the conduction electrons.

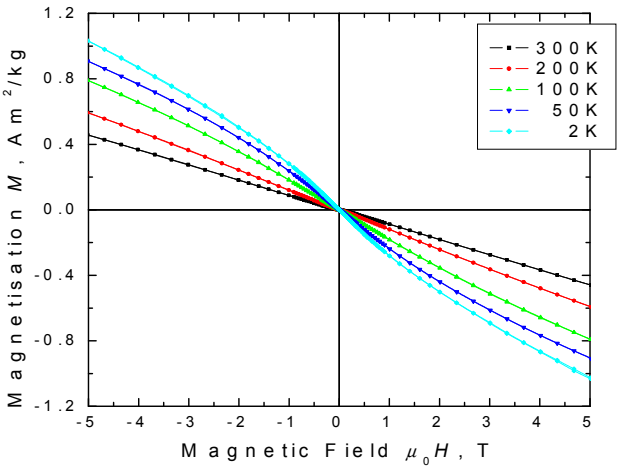

Figure 3-35 Magnetization of carbon nanotubes at different temperatures.

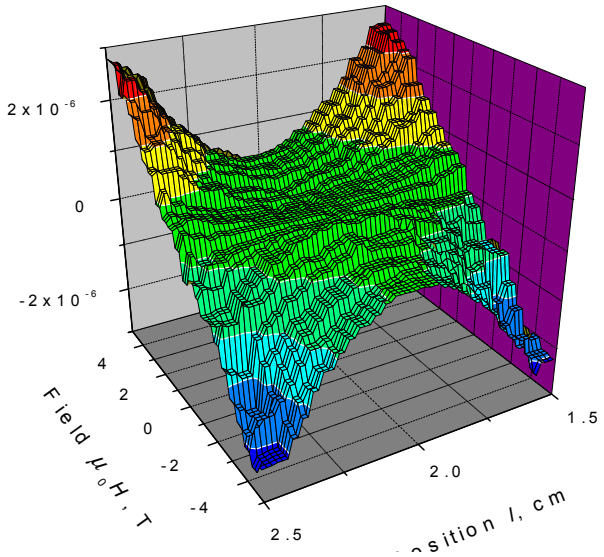

Figure 3-36 Raw SQUID response profile for a nanotubes compact.

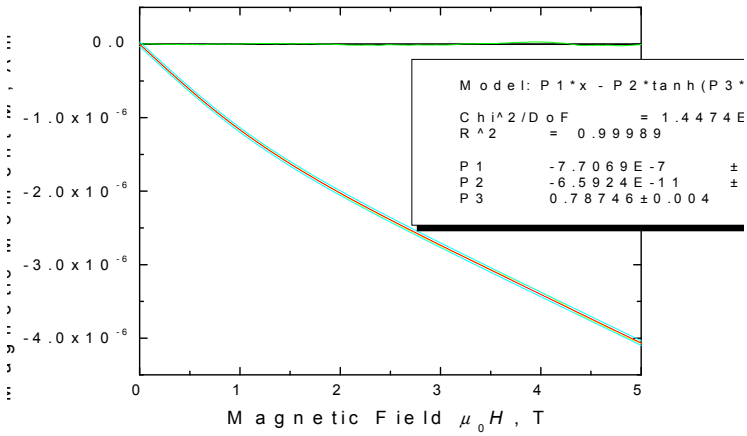

Figure 3-37 Fitting of the magnetization curve to a simple model.

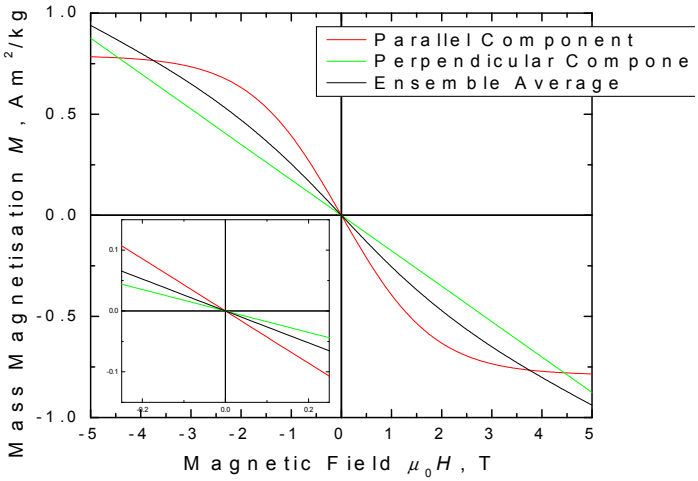

Figure 3-38 Simulation of the magnetization at 5 K.

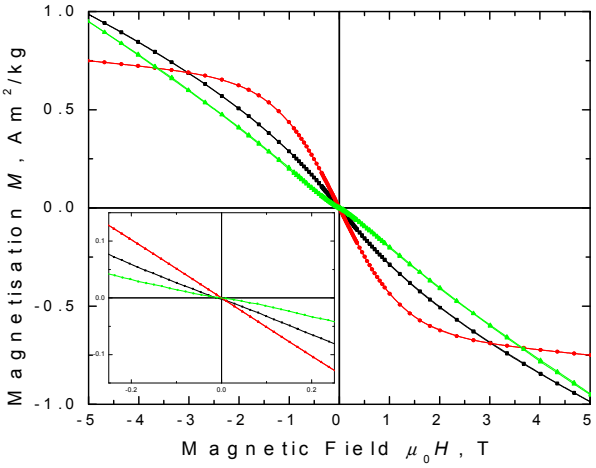

Figure 3-39 Measured magnetization at 5 K.

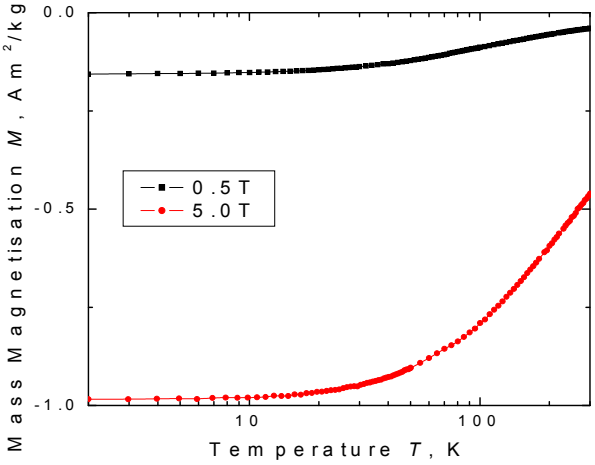

Figure 3-40 Measured temperature dependence of the magnetization.

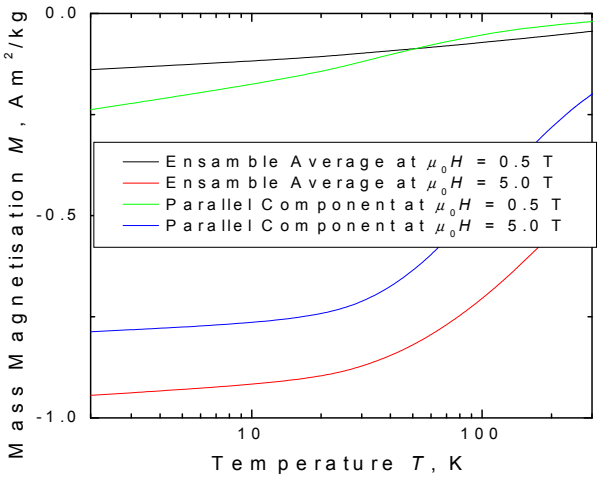

Figure 3-41 Simulation of the temperature dependence of the magnetization.

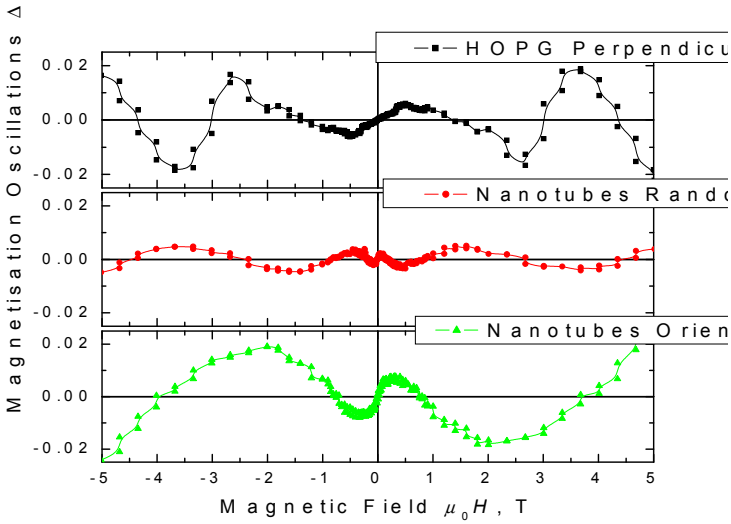

Figure 3-42 Comparison of the dHvA oscillations in HOPG and nanotubes.

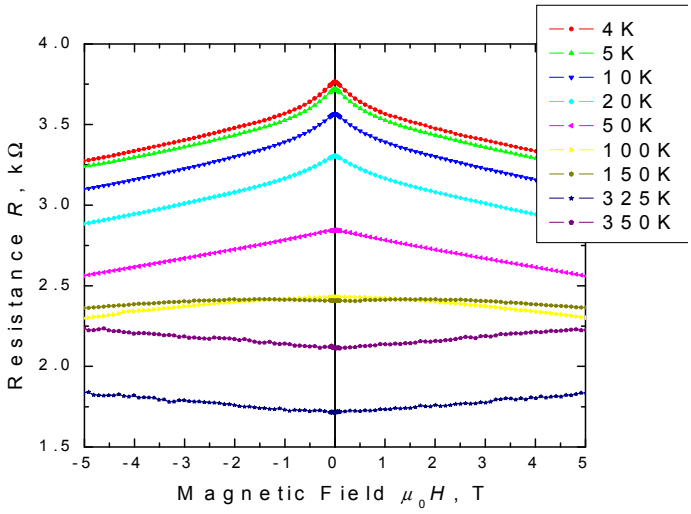

Figure 3-43 Resistance of nanotubes compact at different temperatures.

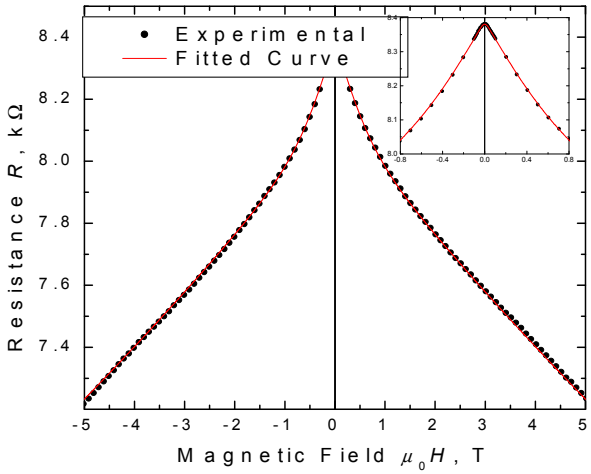

Figure 3-44 Resistance of a nanotubes compact at 1.8 K and a fit to it.

3.2.5 Conclusions on the Magnetism of Graphite and Carbon Nanotubes

A summary of the material parameters extracted follows:

Material	Property	Value	Units	Notes
HOPG	Magnetic susceptibility	$-3.8\ 10^{-7}$	m^3kg^{-1}	Parallel to the *c* axis, 1.8 K
HOPG	Magnetic susceptibility	$-5\ 10^{-9}$	m^3kg^{-1}	Perpendicular to the *c* axis
HOPG	Magnetoresistance	2280	%	Field parallel to *c*, 1.8 K, 5 T
HOPG	Carrier density	$3\ 10^{-4}$	el/atom	At 1.8 K
HOPG	Rel. Phase of HE/MR	$\pi/4$	rad	Dephasing of the oscillations
HOPG	Electron effective mass	0.039	m_e	Majority carriers
HOPG	Anisotropy of m*	25:1		Majority carriers
HOPG	e-Fermi X-section	$4.2\ 10^{16}$	m^{-2}	Majority carriers
HOPG	Fermi level position	12	meV	Bottom of c-band
HOPG	Smallest gap	2	meV	Detected by breakdown
HOPG	Dingle temperature	5	K	Average for ZYB grade
CNT	Magnetoresistance	13	%	Random, 1.8 K, 5 T
CNT	Effective magneton	25	μ_B	Transverse at 1.8 K
CNT	2D band parameter	3	eV	Hopping integral
CNT	Free electron density	$3\ 10^{-5}$	el/atom	At 1.8 K
CNT	Athermal relax. time	100	fs	Ensemble average

As a result of the experimental observations, apart from the material parameters of interest already summarized, the following general remarks should be made:

a) HOPG is indeed a semi-metal with a very small carrier concentration and effective mass.
b) Majority electrons in HOPG have normal 3D (though very anisotropic) dispersion.
c) Majority holes in HOPG might have 2D-like dispersion.
d) Re-entrant metallic state of HOPG at low temperatures and high fields is questionable.
e) No explicit 2D quantum Hall effect was observed.
f) No evidence for superconductivity correlations in HOPG was found.
g) Ferromagnetism is ambiguous (in the defect-less HOPG structure it is either due to impurities or is mimicked by saturating paramagnetic behavior of loose spins in the system).
h) Anomalous diamagnetism and magnetoresistance may be a general feature of macroscopic ensembles of nanotubes.
i) The carriers in multi-walled carbon nanotubes may be spin-polarized.
j) Small effective masses are source for magnetism.
k) No ferromagnetism was observed in multi-walled carbon nanotubes.

4 List of Papers, Oral and Poster Presentations

1) *Measurement of spin-polarization using Schottky junctions* (poster), P. Stamenov and J.M.D. Coey, Boulder Summer School on Magnetism, Boulder, Colorado (2003)
2) *AC susceptibility – theory and application to magnetic measurements* (talk), P. Stamenov and J.M.D. Coey, Boulder Summer School on Magnetism, Boulder, Colorado (2003)
3) *Magnetization of electrodeposited Ni: metastable vacancies and interstitials,* C. O'Reily, S. Sanvito, P. Stamenov, J. M. D. Coey, Submitted (with referees 2004)
4) *Anomalous susceptibility of carbon nanotubes – quantum size effect,* P. Stamenov and J. M. D. Coey, Submitted (with referees 2004)
5) *Magnetic susceptibility of carbon – theory and experiment* (invited talk), P. Stamenov and J. M. D. Coey, To be published in JMMM (JEMS Proceedings, 2004)
6) *Shubnikov de Haas and quantum Hall oscillations in graphite* (talk), P. Stamenov and J. M. D. Coey, To be published in JMMM (JEMS Proceedings, 2004)
7) *Oriented hard magnets prepared by deposition in nano-porous membranes* (poster), N. Chaure, P. Stamenov, F. M. F. Rhen, J. M. D. Coey, To be published in JMMM (JEMS Proceedings, 2004)
8) *Anisotropic ferromagnetism in ZnO* (poster), J. M. D. Coey, M. Venkatesan, C. Fitzgerald, P. Stamenov, L. Dorneles, To be published in JMMM (JEMS Proceedings, 2004)
9) *Magnetism in hafnium dioxide* (poster), J. M. D. Coey, M. Venkatesan, P. Stamenov, C. B. Fitzgerald, L. S. Dorneles, To be published in JMMM (JEMS Proceedings, 2004)

5 List of Experimental Set-ups Developed

5.1 Alternating Field Susceptometer

Kinds of measurements: real and imaginary parts of the magnetic susceptibility as a a function of temperature or frequency.
Field range: 0 – 10 mT.
Temperature range: 280 – 1000 K.
Absolute sensitivity: 10^{-8} Am^2.
Other features: passive magnetic and electric shielding, protective gas atmosphere or vacuum environment.

5.2 Vector Vibrating Sample Magnetometer

Kinds of measurements: 2 components of the magnetic moment vector as a function of applied field magnitude and direction.
Field range: 0 – 2 T in any direction in a horizontal plane.
Temperature range: room temperature.
Absolute sensitivity: 10^{-7} Am^2.
Other features: 3-rd axis second order gradiometer coil.

5.3 High-temperature Magnetic Torsion Balance

Kinds of measurements: torque as a function of temperature and applied magnetic field.
Field range: 0 – 2 T
Temperature range: 300 – 900 K
Absolute sensitivity: 10^{-9} Am^2.
Other features: protective gas atmosphere.

6 Plan of Future Work

Our investigation of the electronic properties of graphite brought us to the conclusion that the pure, defect-less, allotropic form is not ferromagnetic, and exhibits saturation of the magnetisation only due to low temperature and high field paramagnetism. While the active spin-polarized current transport in graphite remains to be investigated, because of the lack of preparation technology for its thin film form, bismuth may take place as potential candidate for semi-metallic spin-polarized current transmitter. The possibility of 'organic' ferromagnetism remains an open question. With the most recent observations of ferromagnetic-like behaviour in proton-irradiated highly oriented graphite, carbon nano-foam, organic-coated gold nano-particles, oxide films, containing no atoms of 3*d* or 4*f* elements, a completely new phenomenon is beginning to arise and take shape.

There is scarce information about the nature of this new type of magnetism. All that is presently known may be summarized as follows:

a) The ferromagnetic-like behaviour is present at room temperature, more over, often as high as 800 K.
b) The magnetic response may be extremely anisotropic – up to a factor of 2 when the solid is crystalline.
c) It may be attributed to defects and/or be purely interfacial property.

The nature of the ground state of all the exemplary systems is not known, nor there is anything clear about what the possible excitations may be. There is a strong demand for a systematic experimental and theoretical investigation of the new phenomenon. Firstly, a rigorous analysis of the existent experimental observations should be made, to build a basis for understanding and bring clarity on the detailed experiments that have to be performed in order to resolve the problem. Secondly, a simple, yet comprehensive theoretical framework has to be developed, to explain the contradictions between the standard 'spins and exchange interaction' paradigm of classical ferromagnetism and the experimental observations and, possibly, to create an entire new way of looking at ferromagnetism, based on orbital moments. The major tasks that have to be accomplished may be classified as follows:

1. Improve an existing Kerr effect and Faraday effect set-ups, to achieve better signal/noise ratio with lock-in detection, gain from an increased sweep rate, and install polarized light sources that can cover a wider spectral range.
2. Design and realize a strip-line ferromagnetic resonance experimental set-up, including electronics, wave-guide system, bias field system, lithographic definition of the measuring lines, and deposition of samples on top of them.
3. Design and realisation of anomalous skin-effect set-up, including electronics, wave-guides and sample mounting assemblies.
4. Develop a theoretical model of interacting orbital moments and investigate the experimentally observable consequences.
5. Collaborate on series of investigations involving very specialized equipment, including ultra-fast pump-probe experiments, neutron diffraction, inelastic neutron scattering, and x-ray magnetic circular dichroism.
6. Develop a model material system and investigate its properties.
7. Analysis of experimental evidences on orbital ferromagnetism and thesis writing.

Month	Task 1	Task 2	Task 3	Task 4	Task 5	Task 6	Task 7
1	Kerr set-up improvement			Development of a theoretical model of interacting orbital moments	Collaborate on a fast optics pump-probe type of experiments		Filter out the existing background of experimental data on the subject
2							
3							
4							
5		Design and realization of a strip-line fast magnetisation dynamics set-up					
6	Develop a Faraday effect set-up						
7						Develop a model material system to serve as a prototype for investigation of the orbital ferromagnetism	
8							
9							
10							
11							
12							
13					Collaborate on neutron diffraction, inelastic neutron scattering, and x-ray circular dichroism experiments		
14							
15			Design and realization of an anomalous skin-effect set-up				
16						Complete characterisation of the model system and analyse the results	
17							
18							
19							
20							Final data analysis and thesis writing
21							
22							
23							
24							

7 Experimental and Sample Preparation Conditions

7.1 Schottky Diodes Preparation

Commercial n-doped Si and GaAs wafers of different cuts (<100>, <111>, etc.) were used as semiconductor substrates. All wafers were cleaned in boiling acetone, boiling methanol and 20 MΩ deionised water. For the Si substrates, standard semiconductor grade etching solution NH_4OH: HF:H_2O was used. The GaAs substrates were sequentially etched in H_3PO_4:H_2O_2:H_2O optimised solution and in HCl:H_2O. All wafers were then washed in deionised water, dried in N_2 and immediately introduced into the vacuum chamber for deposition.

Deposition was done by Ar magnetron sputtering at 10^{-3} mBar (Shamrock Sputtering Tool) or alternatively by thermal evaporation at 10^{-7} mBar (Eduards AUTO 306). All sputtering targets and evaporation sources were of at least 4N purity. Metal layer thickness was 30 nm for the diodes prepared for galvanic measurements, and 15 nm for the diodes prepared for photovoltaic measurements. Consecutively thick Ag contact pads were evaporated for the external contacts on the metallic side.

The Ohmic contacts are prepared by direct soldering with In metal at 400 K and consecutive rapid annealing at 800 K. During the entire process, the metal side of the junctions was cooled by a jet of high-purity Ar gas, in order to avoid oxidation and intermixing and large inter-diffusion of metal atoms, across the interface.

7.2 Galvanic Measurements

DC measurements were performed using the standard 4-wire method with source-meters (Keithley 2400, 2410 and HP228 series). AC measurements were performed using a resistance bridge, with an isolating transformer for the AC/DC decoupling, Lock-in amplifiers (EG&G 52 series), and programmable voltage source (Keithley 240).

The temperature was stabilised using a water bath (Grant) to circulate water through two planar heat sinks, between which the diodes were sandwiched. The temperature was thus stable to within 0.05 K.

Magnetic field was provided with a 5.5 T wide bore superconducting magnet with stability of 0.05% for a period of 1 h. The magnetic field applied was deduced from the energizing current measured as a voltage drop across a high stability shunt.

7.3 Photo-voltaic Measurements

The diodes were illuminated using a fibre-optic assembly, with focusing/de-focusing lenses and collimators. Air-cooled, filtered xenon lamp (XeKL1500) was used as a light source. The magnet and temperature stabilisation assemblies were identical to the ones from point 7.2.

7.4 Graphite and Carbon Nanotubes

The HOPG samples were obtained from the Graphite Research Institute, Moscow, Russia, and Advanced Ceramics (Union Carbide), USA. The samples investigated were

of different grades – ZYA, ZYB and ZYH graphite of nominal 5N5 purity with Mozaic spread of around 0.3^{o} for the best grade. The samples were cut with a diamond blade and cleaved before contacting (for the transport samples) with 30 nm evaporated gold pads.

The multi-walled carbon nanotubes used were produced by the standard He ark technique from 5N5 pure graphite ingot, and were on average 1-3 μm long, with a mean diameter around 20 nm.

7.5 Magnetisation Measurements

Magnetisation measurements were performed on a SQUID magnetometer (Quantum Design XL 5). The maximal applied field was 5 T with reproducibility of around 0.01 mT. The temperature was controlled with a He vapour-flow cryostat in the range 1.7 – 300 K. The samples were mounted in clear drinking straws using gelatine capsules, ensuring that no air was trapped in the sample space (oxygen is strongly paramagnetic at low temperature).

7.6 Transport Measurements

Transport measurements at small fields (up to 5T) were performed in system described in point 7.5, using a resistance bridge (Linear Research-200 series) and source-meter (Keithley 2400).

Transport measurements at high fields (up to 23 T) were performed at Grenoble High Magnetic Field Laboratory (magnet site M3), using two different set-ups – a He4 bath cryostat with a biaxial rotation stage, and a He3 cryostat with uniaxial rotation stage, in the temperature range 0.3 – 5 K. Vernier Lock-in (EG&G 58 series) detection was used with an arbitrary DC bias for removal of the zero-bias contact abnormalities.

8 References

[1] Rhoderick, E. Huw, "Metal-Semiconductor Contacts", 2nd ed.(1988)
[2] M. Ziese and M. J. Thornton (Eds.), "Spin Electronics", Springer-Verlag (2001)
[3] P. Esquinazi, Phys. Rev. B, **66**, 024429 (2002)
[4] H. Kempa, Y. Kopelevich, F. Mrowka, A. Setzer, J. H. S. Torres, R. Hohne, P. Esquinazi, Solid State Comm., **115**, 539 (2000)
[5] O. Cespedes, at. al. J. Phys.: Cond. Mat., **16**, L155 (2004)
[6] D. Ostling, D. Tomanek, and A. Rosen, Phys. Rev. B, **55**, 20, 13980 (1997)
[7] L. Landau, E. Livshitz, "Electrodynamics", 2nd ed. (1982)
[8] A. Bachtold, at. al., Nature, 397, 673 (1999); A. Fujiwara, K. Tomiyama, H. Suematsu, Phys. Rev. B, **60**, 13492 (1999)
[9] H. Ajiki, T. Ando, J. Phys. Soc. Japan, **62**, 2470 (1993); T. Ando, T. Nakanishi, M. Igami, J. Phys. Soc. Japan, **68**, 3994 (1999)
[10] E. Minot, Y. Yaish, V. Sazonova, P. L. McEuen, Nature, **428**, 536 (2004)
[11] J. Heremans, C. H. Olk and D. T. Morelli, Phys. Rev. B , **49**, 15122 (1994)
[12] A. Ramirez, at. al, Science, **265**, 84 (1994)
[13] V. Likodimos, S. Glenis, N. Guskos, C. L. Lin, Phys. Rev. B, **68**, 045417 (2003)
O. Chauvet, L. Forro, Phys. Rev. B, **52**, R6963 (1995); S. Bandow, J. Appl. Phys. **80**, 1020 (1996); F. Tsui, L. Jin, O. Zhou, Appl. Phys. Lett., **76**, 1452 (2000)
[14] A. S. Kotosonov, S. V. Kuvshinnikov, Phys. Lett. A, **229**, 377 (1997); A. S. Kotosonov, JETP Letters, **70**, 476 (1999)
[15] J. M. Ziman, "Principles of the Theory of Solids", Cambridge (1965)
[16] P. Byszewski, J. Phys. Chem. Solids, **58**, 11, 1685 (1997)
[17] R. Saito, G. Dresselhaus, M. Dresselhaus, Imperial College Press (1998)
[18] J. M. D. Coey, J. Appl. Phys., **85**, 5576 (1999)